Nocturnal Cold-Air Intrusions into a Closed Basin: Observational Evidence and Conceptual Model

C. DAVID WHITEMAN, SEBASTIAN W. HOCH, AND MANUELA LEHNER

University of Utah, Salt Lake City, Utah

THOMAS HAIDEN

Central Institute for Meteorology and Geodynamics, Vienna, Austria

ABSTRACT

Observations are analyzed to explain an unusual feature of the nighttime atmospheric structure inside Arizona's idealized, basin-shaped Meteor Crater. The upper 75%–80% of the crater's atmosphere, which overlies an intense surface-based inversion on the crater's floor, maintains a near-isothermal lapse rate during the entire night, even while continuing to cool. Evidence is presented to show that this near-isothermal layer is produced by cold-air intrusions that come over the crater's rim. The intrusions are driven by a regional-scale drainage flow that develops over the surrounding inclined Colorado Plateau. Cold air from the drainage flow builds up on the upwind side of the crater and splits around the crater at low levels. A shallow layer of cold air, however, spills over the 30–60-m-high rim and descends partway down the crater's upwind inner sidewall until reaching its buoyancy equilibrium level. Detrainment of cold air during its katabatic descent and compensatory rising motions in the crater atmosphere destabilize the basin atmosphere, producing the observed near-isothermal lapse rate. A conceptual model of this phenomenon is presented.

1. Introduction

The depths and strengths of temperature inversions in valleys and basins generally increase during the night, so that, by sunrise, a deep high-stability layer extends all the way to the ridge top (see, e.g., Whiteman et al. 1996). Our recent study of temperature inversion evolution at Arizona's Meteor Crater, however, found an unusual temperature structure in the crater atmosphere on synoptically undisturbed nights (Whiteman et al. 2008) characterized by a deep near-isothermal layer in the upper 75%–80% of the crater atmosphere overlying an intense near-surface inversion. This structure persisted through the night even as the atmosphere continued to cool. Persistent near-isothermal temperature structures such as this have not been reported before in other similar-size basins such as the Sinbad Basin (Whiteman et al. 1996), the Peter Sinks Basin (Clements et al. 2003), or the Gruenloch Basin (Steinacker et al. 2007). The

processes responsible for the production and maintenance of the persistent near-isothermal layer are the subject of this paper. This topic is addressed through analysis of meteorological data from the Meteor Crater, leading to a conceptual model that will be tested further using analytical and numerical models in a follow-on paper.

This paper is organized into 6 sections. Following the introduction in section 1, the topography of the Meteor Crater and the meteorological data are introduced in section 2. The temperature structure and auxiliary data are analyzed to develop and test hypotheses regarding the origin and maintenance of the near-isothermal layer in section 3. Based on these analyses, a conceptual model of the phenomenon is presented in section 4. Several remaining issues regarding the phenomenon are discussed in section 5, and a summary and conclusions are presented in section 6.

2. Meteor Crater topography and the meteorological data

a. Topography

Arizona's Meteor Crater (Fig. 1), located 40 km east of Flagstaff, Arizona, was produced approximately 50 000

Corresponding author address: C. David Whiteman, Department of Atmospheric Sciences, University of Utah, 135 S 1460 E, Rm. 819, Salt Lake City, UT 84112-0110.
E-mail: dave.whiteman@utah.edu

FIG. 1. Aerial photograph of Meteor Crater, Arizona, in the early morning looking across the crater toward the northwest. The photograph is courtesy of J. Shelton, used with permission.

years ago by the impact of a meteorite (Kring 2007). The idealized, circular, basin-shaped crater, 170 m in depth and 1.2 km in diameter, is thought to be the best preserved meteorite crater on earth. The unbroken rim of the crater extends 30–60 m above the surrounding Colorado Plateau, a uniform plain that slopes gently upward to the Mogollon Rim 30 km to the southwest of the crater.

b. Meteorological data

Meteorological data come from the Meteor Crater Experiment (METCRAX) field program of October 2006. The data to be used in this paper (Fig. 2) include sonic detection and ranging (sodar) and flux tower data from the southwest (SW) site 2.5 km southwest of the crater center; data from four lines of temperature dataloggers running from the crater floor center up the north, east, south, and west sidewalls over the rim and out onto the adjacent plain; data from three tethersondes operated on an east–west line across the crater floor and sidewalls; data from two flux towers located on the crater's west sidewall; and data from three towers on the crater rim. Additional information on the instrumentation, field sites, and data processing is available from the METCRAX experiment overview paper (Whiteman et al. 2008).

3. Analysis of data

Analyses focus primarily on the night of 22–23 October 2006, a night with clear skies in which synoptic-scale winds above Meteor Crater were very weak, and on the night of 26–27 October 2006, when the synoptic winds above the crater were northerly at speeds up to 10 m s^{-1} before midnight and became northerly or northeasterly at speeds of only 2 m s^{-1} in the second half of the night.

a. Temperature structure evolution in the crater

The temperature structure evolution during the night of 22–23 October 2006 is illustrated in Fig. 3 using tethersonde data from ascents made from the center of the crater floor. Astronomical sunset was at 1738 mountain standard time (MST) but, because of the propagation of shadows from the crater rim, local sunset at the central tethersonde site was at 1606 MST. The atmosphere in the crater was well mixed and coupled to the atmosphere over the Colorado Plateau at 1600 MST. The sounding at this time revealed a shallow superadiabatic layer on the crater floor surmounted by a neutral layer that extended through the depth of the crater and into the atmosphere above. By 1730 MST, a weak 25-m-deep stable layer formed over the crater floor. Between about 1730 and 1942 MST, the top of the stable layer rose slowly as the stability of the atmosphere increased (see arrows in Fig. 3). This initial increase in stable layer depth is similar to that seen in other valleys and basins and is thought to be caused by the convergence of downslope flows on the valley floor and the buildup of a cooled air mass in the basin. At the same time that the top of the stable layer was rising, a shallow surface-based inversion sublayer intensified on the crater floor. By 2030 MST the profiles had obtained a vertical structure that featured a 30–50-m-deep, surface-based, intense, inversion sublayer on the crater floor that was surmounted by a near-isothermal layer that occupied the upper 75%–80% of the crater's depth. During the remainder of the night, the air within the crater continued to cool, while maintaining this same basic vertical temperature structure. Because of the more rapid cooling inside the crater compared to that of the atmosphere above the crater, a temperature jump developed gradually at the level of the crater rim later in the night. The processes responsible for the persistence of the near-isothermal layer are the main focus of this paper.

Two additional tethersondes were operated concurrently with the one at the crater center. These tethersondes were flown from the lower east and west sidewalls from positions 22 m above the crater floor. These starting heights meant that the east and west tethersondes began their ascents near the top of the shallow, intense, surface-based inversion that formed on the crater floor. Synchronous temperature profiles from the three tethersondes (Fig. 4) showed similar temperatures and persistent near-isothermal lapse rates throughout the night, indicating that the near-isothermal layer was horizontally homogeneous across the crater basin.

The persistence of the deep near-isothermal layer, a feature unique to the Meteor Crater in comparison with other basins previously studied (see section 1), suggests
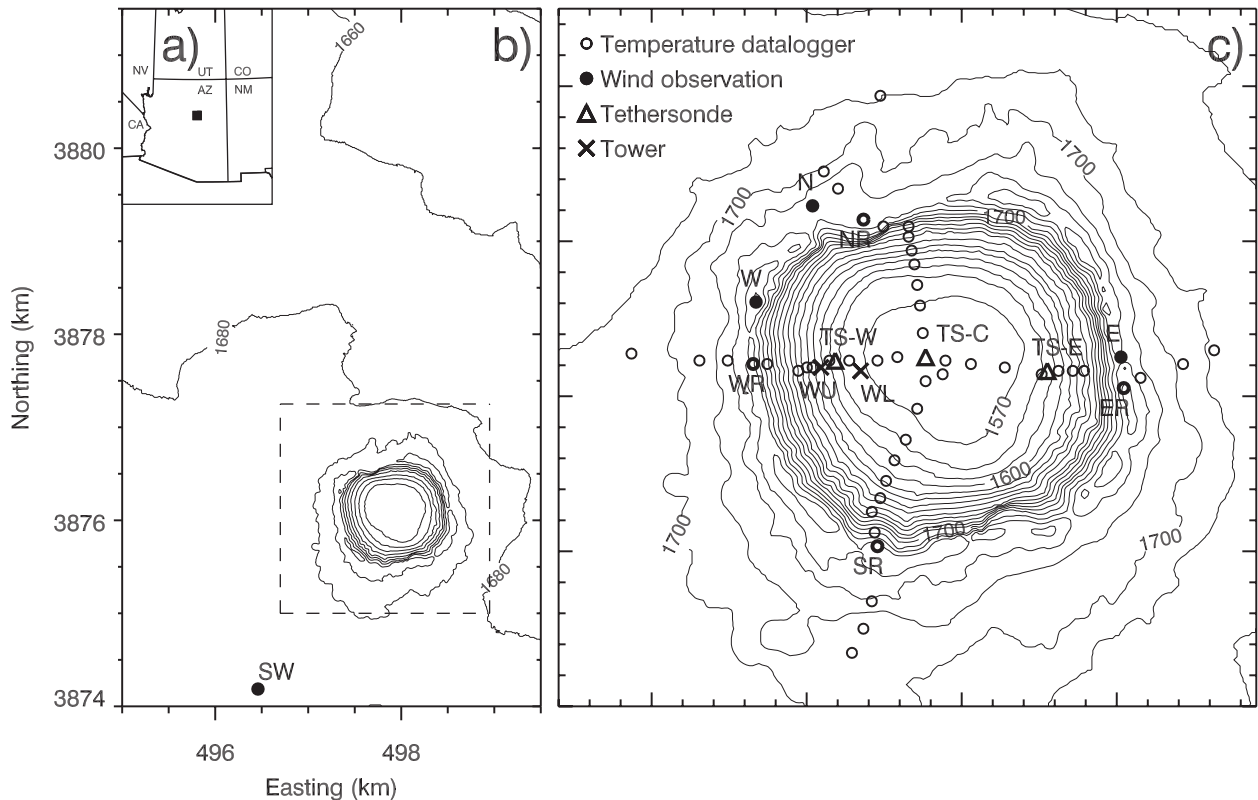
FIG. 2. Universal transverse Mercator zone 12S map of Meteor Crater showing the meteorological instrumentation sites. (a) Location of Meteor Crater in Arizona; (b) location of the SW site relative to Meteor Crater, with 20-m altitude contours; and (c) location of instrumentation in and immediately around Meteor Crater, with 10-m altitude contours. Temperature datalogger lines, indicated by open circles, run up the north, east, south, and west sidewalls of the crater, extending over the rim and onto the adjacent plain. The boldface open circles indicated as NR, ER, SR, and WR are the temperature dataloggers on the north, east, south, and west rim, respectively. Anemometers on the west, north, and east rims are indicated by filled circles labeled W, N, and E, respectively. Tethersondes were flown from sites indicated with triangles on an east–west line through the crater labeled tethersonde west (TS-W), tethersonde central (TS-C), and tethersonde east (TS-E). Flux tower locations on the west sidewall are indicated with an X and labeled WU and WL.

that a continuous destabilization process must be present in the crater atmosphere. Two such processes are immediately brought to mind: a vertical shear of horizontal wind across the basin atmosphere would drive the atmosphere toward neutrality (i.e., a dry-adiabatic lapse rate), and radiative processes (especially vertical divergence of longwave radiative fluxes) would drive the atmosphere toward isothermalcy. A separate study of radiative transfer in the crater using a three-dimensional Monte Carlo radiative transfer model (S. W. Hoch 2009, personal communication) indicates that the time scale and magnitude of radiative flux divergence is insufficient to account for the observed destabilization. In the next section we will investigate the wind field in the crater to test the shear hypothesis.

b. Evolution of the wind field in the crater

Winds within the crater on the night of 22–23 October became light (generally <1 m s^{-1}) and variable in direction once the crater atmosphere became stably stratified (Fig. 5). On the east side of the crater (Fig. 5c), the winds died completely and remained quiescent throughout the night. Winds were also weak (generally <1.5 m s^{-1}) at the central (Fig. 5b) and west (Fig. 5a) tethersonde sites, but the winds progressively expressed a more turbulent character as the west sidewall was approached. The stronger, larger-scale winds that were present above the crater during nighttime did not intrude into the crater, so that a strong wind shear occurred only at and above the crater rim. Because winds were light in the crater atmosphere and vertical shear was not present across the depth of the crater basin, we reject the hypothesis that the destabilization was produced by vertical shear of horizontal winds within the basin. Since both the radiative and shear hypotheses have been rejected, further analysis to determine the cause of the destabilization focused on near-surface temperature and wind observations on the west sidewall
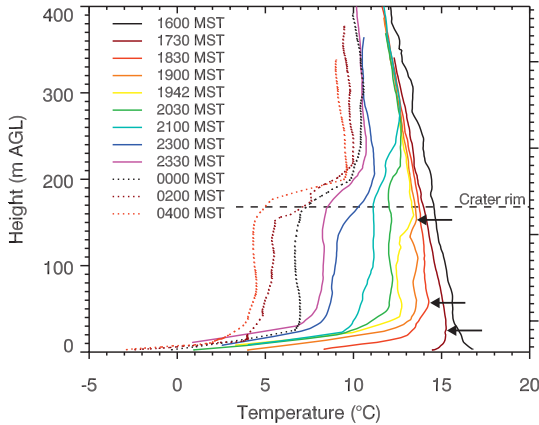
FIG. 3. Selected tethersonde soundings from the crater floor center (TS-C) illustrating temperature profile evolution during the night of 22–23 Oct 2006. Sounding times are given in the legend. Arrows illustrate the rapid rate of rise of the stable layer in the early evening.
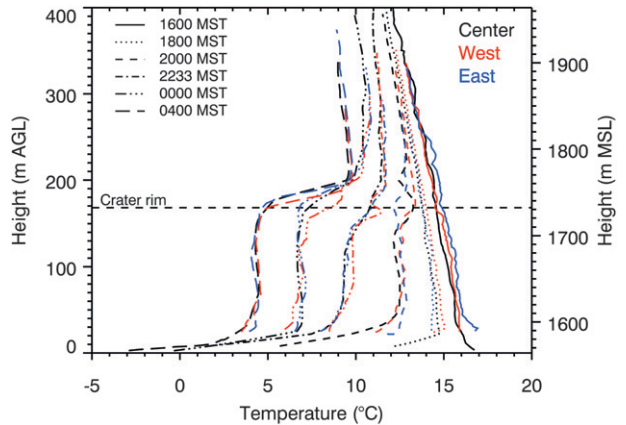
FIG. 4. Synchronous temperature profiles from the TS-C, TS-W, and TS-E tethersonde sites, 22–23 Oct 2006.

of the crater where the turbulent motions appeared to be strongest.

c. Near-surface temperature and wind observations

Pseudovertical soundings from four lines of temperature dataloggers running up the north, east, south, and west sidewalls and out onto the adjacent plain were analyzed to visualize the temperatures and temperature gradients during the night in the near-surface layers. Temperature measurements on these lines were taken at heights of 1.2 m above ground level at 5-min intervals. The temperature data were combined with wind data from the west, north, and east rims and from a 10-m tower 2.5 km southwest of the crater center on the adjacent plain to produce Fig. 6. Pseudovertical soundings from the lines of temperature dataloggers are shown in

Fig. 6a for 2055 MST 22 October. At this time, winds on the Colorado Plateau outside the crater were from the southwest (see southwesterly wind at site SW), while winds at the crater rim were westerly. These southwest winds are a typical nighttime feature at Meteor Crater during undisturbed nights. They represent a regional-scale cold-air drainage flow that arrives down a mean 2° slope from higher terrain about 30 km to the southwest of the crater. A modeling study by Savage et al. (2008) showed that the regional-scale drainage flow produces peak winds of 3–5 m s^{-1} at heights of 30–50 m AGL above the sloping Colorado Plateau in the vicinity of Meteor Crater. Temperatures at the south and west rim (Fig. 6a) are several degrees colder than at the north and east rim, illustrating the effects of the cold-air advection in the regional-scale drainage flow. The intense surface-based inversion at the crater floor is seen in all four lines of pseudovertical temperature profiles, but the profiles on the south and west lines are distinctly
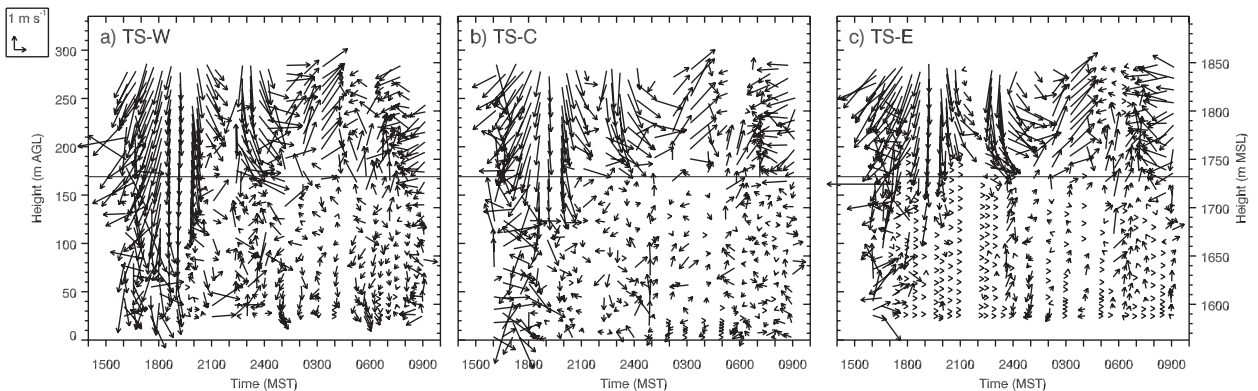
FIG. 5. Time–height cross sections of horizontal vector winds from the (a) TS-W, (b) TS-C, and (c) TS-E tethersonde sites, 22–23 Oct 2006. A vector pointing straight up would be a wind from the south, a vector from right to left would be an east wind, etc. The thin horizontal lines indicate the mean rim level.
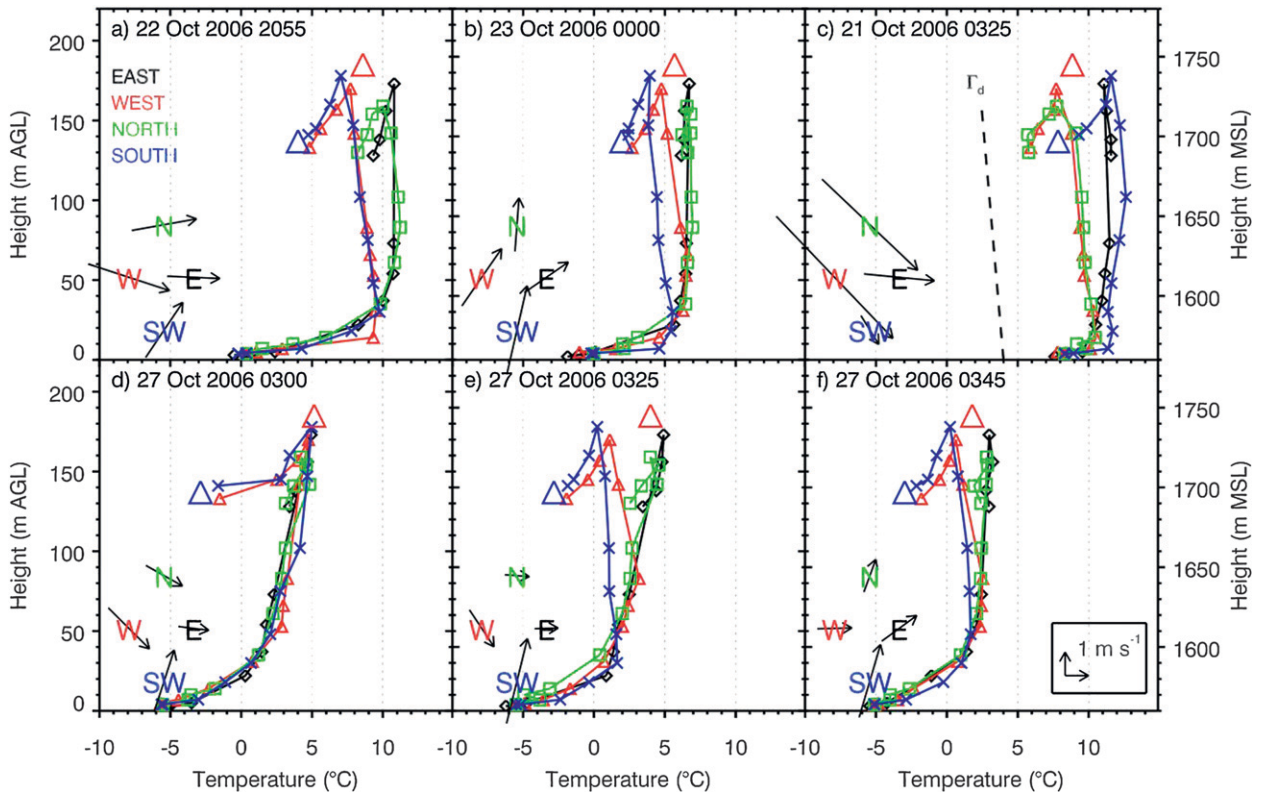
FIG. 6. Pseudovertical temperature profiles from four lines of temperature dataloggers running up the north (green), east (black), south (blue), and west (red) inner sidewalls of the crater to the rim level and out onto the adjacent plain. Vector winds from the 5-m level at the N and E rim sites, and from the 10-m level at the W rim site and at the SW site on the plain outside the crater are plotted schematically (not to scale) in the lower-left part of each subfigure. The large red and blue triangles indicate 2-m temperatures at the WR and at the SW site. For reference, the dry-adiabatic lapse rate Γ_d is shown in (c).

different from the profiles on the north and east lines. The north and east lines have near-isothermal lapse rates, in agreement with the tethersonde soundings inside the crater. The south and west lines, on the other hand, exhibit a superadiabatic temperature profile, with a lapse rate of about $15°C\,km^{-1}$. The convergence of the superadiabatic and near-isothermal profiles at the top of the intense surface-based inversion at the crater floor defines a V-shaped notch with the isothermal profile on the right and the superadiabatic profile on the left. This V-shaped notch is a common feature of temperature profiles in the crater on clear nights when synoptic-scale flows are weak.

The temperature profiles reveal further information about the temperature structure outside the crater. The temperature profile on the upwind outer sidewall of the crater shows the buildup or accumulation of cold air upwind of the crater. This buildup, which is accompanied by a splitting of low-level flow around the crater and an advection of cold air over the upwind rim of the crater is seen in drainage flow simulations with the Kaltluftabflussmodel (KLAM_21) drainage flow model

of the German Weather Service (M. Kossmann 2009, personal communication). Cold air that surmounts the upwind rim of the crater, because it is colder than the air in the crater at the same height, will descend into the crater down the upwind inner sidewall. In contrast, the temperature lapse rate on the downwind outer sidewall of the crater is often similar to the lapse rate on the downwind inner sidewall (see, e.g., Figs. 6b–f), presumably because a wake forms downwind of the crater keeping cold air displaced away from the outer slope. There will be a tendency for descent of the outflow down the downwind outer sidewall to be at the dry-adiabatic lapse rate, although the lapse rate will be affected by heat transfer to the underlying ground and mixing with the ambient atmosphere. An equal mass of air must flow out of the crater over the downwind sidewall as flows into the crater over the upwind rim.

The temperature deficit between the cold, negatively buoyant air descending the upwind inner sidewall and the bulk of the crater atmosphere (as indicated by the north and east temperature profiles) decreases with downslope distance (Fig. 6a). Thus, we can interpret the width of the

V at the rim as the temperature deficit of the intrusion air, while the apex of the notch, marks the altitude where the cold-air inflow on the slope reaches its level of buoyancy equilibrium and dissipates or leaves the slope. Thus, the inflow air gradually loses negative buoyancy as it descends. The V-shaped notches produced by the intersection of the south or west profiles with the north or east profiles occur at about the same elevation on the south and west lines in Fig. 6a. There are, however, many instances when the apex of the V-shaped notch varies in elevation on the different datalogger lines. In Fig. 6b at 0000 MST 23 October, for example, the apex of the V-shaped notch reaches within 20 m of the floor on the south line and within 70 m on the west line. This difference in apex altitudes on the datalogger lines corresponds to a shift in the approaching wind direction from southwest to south-southwest, as seen by the wind vector at the southwest site. Thus, the datalogger line with the deepest notch occurs on the line that is most closely aligned with the upwind direction, as the coldest air and strongest inflow is in the upwind direction. As an example, Fig. 6c shows an event on a different night when the drainage flow was affected by a synoptic flow and came from the northwest. In that case, the superadiabatic side of the V notch occurred on the west and north sidewalls, rather than on the south and west sidewalls. Thus, the deepest penetration of the intrusion air occurs on the upwind inner sidewall, with correspondingly lesser penetration at angles away from the upwind direction.

The rate of cooling and the destabilization of the bulk crater atmosphere are strongly affected by cold-air intrusions. The stability of the crater atmosphere increases when no inflow occurs; conversely, the initiation of an inflow quickly destabilizes the crater atmosphere and produces a near-isothermal profile. This is illustrated in Figs. 6d–f for the night of 27 October. At 0300 MST (Fig. 6d), inflow was not present (i.e., no V) and a strong temperature gradient of $22°C\ km^{-1}$ had built up within the crater. This temperature gradient is similar to nighttime temperature gradients in other basins and valleys that have been previously studied (Whiteman et al. 1999). The temperature gradient increased to $27°C\ km^{-1}$ by 0325 MST after an inflow from the southwest (as indicated by the notches in Fig. 6e) began at 0305 MST. This inflow, which began after synoptic-scale northerlies decayed above the crater region, then destabilized the crater atmosphere causing the temperature gradient to decrease to $5°C\ km^{-1}$ by 0345 MST (Fig. 6f).

The bulk cooling of the crater atmosphere has several sources. Background cooling would occur from longwave loss from the crater surfaces and resultant radiative and turbulent sensible heat flux divergences regardless of whether there was an intrusion. The import and assimilation of cold air coming over the rim adds to this background cooling. In synoptically undisturbed situations, the regional-scale drainage flow continues to provide negatively buoyant air at the upwind rim of the crater during the entire night. The distribution of the cooling in the basin atmosphere and the resultant changes to atmospheric stability depend on the cooling mechanism. Cooling would be produced in the stable crater atmosphere by rising motions that compensate for the sinking motions associated with both the cold-air intrusion and any normal katabatic flows from the sidewalls that are undisturbed by the intrusion. The distribution and amount of cooling depend on the altitudinal distribution of rising motions, the atmospheric stratification, and the distribution of basin air mass with height. The main factor producing the destabilization of the crater atmosphere and a significant factor in the overall basin cooling is *detrainment* of cold air from the intrusion layer flowing down the upwind inner sidewall. This occurs in a shallow layer over the slope since neither the temperature nor the wind profiles in the ambient crater atmosphere show cold air entering horizontally. The altitude of the apex of the V-shaped notch in the datalogger temperature profiles represents the distance over which the cold air coming over the rim is fully detrained into the crater atmosphere. The depth of penetration is expected to be governed by the volume flux and temperature deficit of the cold air coming over the rim and the ambient temperature gradient inside the crater. The rate of detrainment must decrease with distance down the sidewall for the observed destabilization to occur from this mechanism. Support for this concept of detrainment of negatively buoyant air flowing down a slope into a stably stratified environment comes from recent laboratory experiments by Baines (2001, 2005). We hypothesize that *the isothermal atmosphere inside the crater is caused by the detrainment and horizontal mixing into the crater atmosphere of cold air that comes over the rim of the crater and flows down the inner sidewall of the crater.* Rising motions over the basin center that compensate for the downward mass transport in the cold-air intrusion layer would also play a role in basin cooling and, with variations in vertical motions with height, destabilization of the basin atmosphere.

Intrusion air descending from the rim would warm at the dry-adiabatic rate of $9.8°C\ km^{-1}$, if there were no heat exchange with the underlying ground or the ambient overlying atmosphere. But the along-slope lapse rate is, instead, *superadiabatic*, typically about $15°C\ km^{-1}$. This suggests that, in addition to the postulated detrainment of cold air into the ambient environment, there is some entrainment of ambient air into the intrusion layer, decreasing its negative buoyancy. This concept of
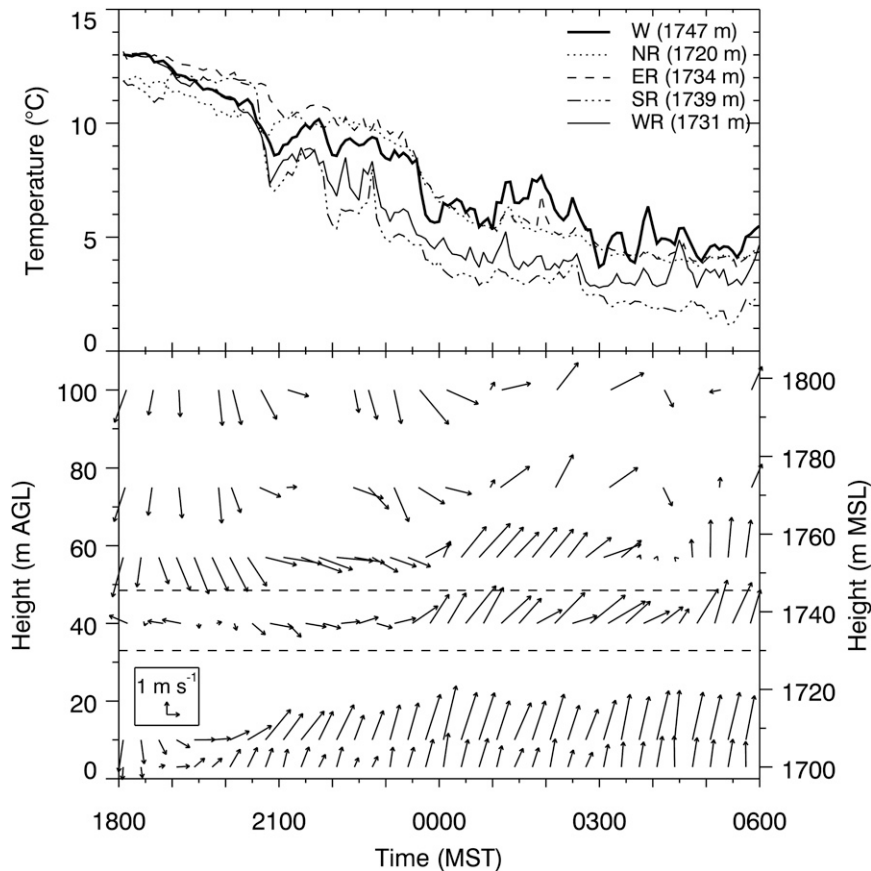
FIG. 7. Temperature and vector wind times series from 1800 MST 22 Oct to 0600 MST 23 Oct 2006. The 0 height datum is SW (1697 m MSL). Temperature data are from the NR, ER, SR, and WR temperature dataloggers and from the 2-m level at W. The legend indicates the MSL heights of the measurements at these sites. Wind vectors are shown for the 3- and 10-m levels of the SW flux tower (5-min average winds plotted every 20 min for legibility), for the first or 40 m sodar range gate at SW (10-min average winds plotted every 20 min for legibility), for the 10-m level at W (57 m above SW), and for the 75- and 100-m levels above SW using occasional tethersonde soundings from TS-C, the central tethersonde site. The two dashed lines indicate the minimum and maximum elevations on the southwest or upwind portion of the rim.

simultaneous entrainment into and detrainment from a negatively buoyant flow on a slope is also supported by laboratory experiments (Baines 1999). The descending flow is unable to completely penetrate to the crater floor. The temperature deficit of the intruding air is too small, the rate of exchange of heat with the ambient atmosphere is too large, and the ambient stability is too great. The intrusion, however, can sometimes descend far enough into the crater to depress the inversion top and push the cold-air pool away from the upwind slope (Figs. 6a–c). This displacement of the cold-air pool and the mixing associated with it can cause short-term temperature rises on the crater floor (Whiteman et al. 2008, their Fig. 7). Other data (not shown) suggest that gravity waves may be generated at the top of the inversion by the impact of the intrusion air.

d. Wind field upwind of the crater and at the rim

Vertical profiles of temperature deficit and wind speed above the rim would be necessary to fully document the cold-air inflow to the crater. Unfortunately, detailed measurements of this type were not made as part of METCRAX 2006. There are, nonetheless, supporting data that tell us much about the inflow and the wind fields around the crater.

Before discussing the inflow, it is important to point out the consistent outflow over the downwind or east rim (E) of the crater in Fig. 6. There are also times when an outflow is seen at the north rim (N), especially when the southwesterly drainage winds shift more into the south (Figs. 6b,f). These outflows are necessary to maintain the crater atmospheric mass balance given the inflow of

cold negatively buoyant air over the upwind rim. The north rim site, however, often sees weak or southwesterly winds produced by splitting of the low-level airflow around the crater (e.g., Fig. 6a).

The regional-scale drainage flow at Meteor Crater is deeper than the crater rim and, like other drainage flows (e.g., Whiteman and Zhong 2008), is stratified (cf. temperatures on the plain and at the crater rim in Fig. 6). If air lifted over the crater rim is colder than that within the crater at the same height, it will descend into the crater. But, with increasing height above the crater rim, the drainage flow may sweep across the entire crater so that no horizontal temperature gradient is present between the crater exterior and interior and no negative buoyancy will be present to cause air to descend into the crater. This suggests that intrusions of cold air into the crater will be shallow and concentrated at elevations near and just above rim height, with the drainage flow above this shallow layer simply advected over the crater. In this section, we wish to estimate the depth of the intrusions. We begin by looking at data on the drainage flow upwind of the crater.

Wind data upwind of the crater are available from a sodar and the 3- and 10-m tower levels at the southwest site. These data, along with temperature data from the north, east, south, and west rim dataloggers (NR, ER, SR, and WR) and from the west rim tower (W in Fig. 2) and wind data from the 10-m level of the west rim tower are shown for 22–23 October in Fig. 7. Unfortunately, because a nearby lightning strike damaged some of the acoustic transducers at the southwest sodar, we are confident only in data from the first sodar range gate at 40 m. A weak southwest drainage flow first appeared at 1920 MST at the 3-m level of the tower at the southwest site (Fig. 7). The flow deepened to encompass the 10-m level of the tower by 2000 MST. The 10-m-level flow suddenly strengthened at 2040 MST, at the same time that winds shifted from northerly to westerly at rim level (at SR, WR, and W) and strengthened. This onset of the regional-scale drainage flow occurred about three hours after astronomical sunset. The backing of winds from south-southwesterly at the surface to southwesterly or westerly at the rim is characteristic of many nights (e.g., see Fig. 6). On this night the winds at rim level turned from westerly into a more southwesterly direction and strengthened following midnight. The regional-scale drainage flow had a katabatic jetlike character with the highest speeds measured at the 10-m level. Unfortunately, the height of the jet maximum and the maximum speed could not be resolved well with the existing data. This regional-scale drainage wind profile is, however, consistent with the modeling results of Savage et al. (2008) whose simulations found the maximum speed of 3–5 m s^{-1}

at 30–50 m above the plain. This predicted height of the jet maximum is about the height of the crater rim, which varies from 33 to 57 m above the southwest site.

The onset of the regional drainage flow led to a sharp decrease of temperature at the south and west rim sites (Fig. 7), but with a lesser decrease at the west rim tower. Once temperatures fell at the south and west rim sites, they remained several degrees Celsius below those at the north and east rim sites. The lowest temperatures (thus, biggest temperature deficits) were seen on the upwind side of the crater and the deepest intrusions were found on the south and west sidewalls (Figs. 6a,b). After 2340 MST the wind direction at 40 m above the SW site and at the west tower anemometer shifted to southwest (Fig. 7). After about midnight temperatures at the west rim tower rose to match those at the north and east rim, indicating that the cold-air inflow over the south and west rims, which had initially been deep enough to encompass the west rim tower, no longer extended vertically to the west rim tower only 8–13 m higher than the south and west rims. Thus, only the lowest part of the drainage flow on the upwind (south and west) side of the crater was cold enough to intrude into the crater basin.

e. Mean and turbulent flow structure in the intrusion layer on the upwind inner sidewall

Data from two flux towers on the west sidewall of the crater were used to analyze the vertical structure and near-surface characteristics of the cold-air inflow (Fig. 8). The towers were installed 38 m [west upper (WU)] and 8 m [west lower (WL)] above the crater floor. Anemometers were located at the 0.5-, 1.5-, 3-, and 5-m levels and additionally at the 8.5-m level on the west lower tower. As shown above, the depth to which the incoming cold air descends on a certain sidewall varies with the direction of the regional-scale flow on the plain surrounding the crater basin and with the temperature deficit of the incoming air. Thus, while cold air intruded into the crater continuously during the night of 22–23 October, the record at west upper shows intermittency in cold-air intrusion events, with a decrease in events after midnight as the approaching winds shifted more into the south. The intruding air, as indicated by the V-shaped notch in the pseudovertical profiles, often reached its level of buoyancy equilibrium before penetrating as far down as the west upper tower. The first intrusion event visible at the tower occurred around 2100 MST when the V-shaped notch reached to within about 10 m of the crater floor (see Fig. 6a). The intrusion resulted in a sharp increase in wind speed at all four levels of the tower (not shown), with the highest wind speed (~4 m s^{-1}) at the topmost level, and with the wind
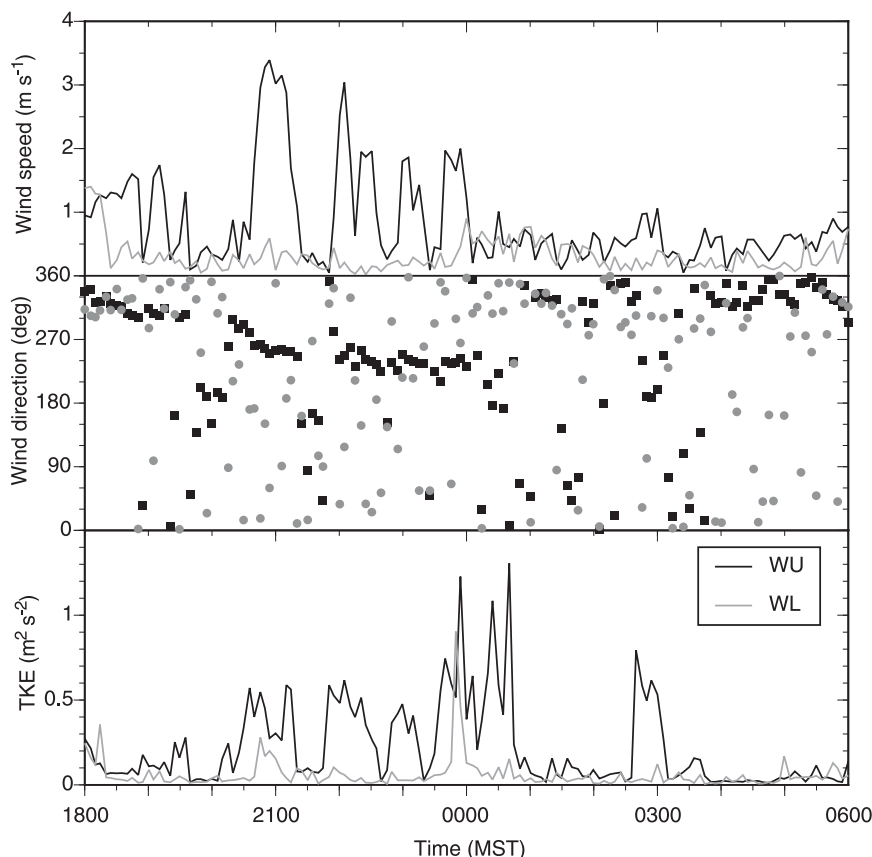
FIG. 8. Wind speed, wind direction, and TKE at 3 m AGL for the night of 22–23 Oct 2006 for the WU (black lines and filled squares) and WL (gray lines and filled circles) flux towers.

direction west-southwest at all tower levels. While the wind direction during nonintrusion periods turned with height, frequently from west to north, it remained constant with height during intrusion periods. All four height levels were within the cold-air intrusion, indicating that its depth exceeded the 5-m tower height. Turbulence was produced by the cold airflow, with turbulent kinetic energy (TKE) increasing from an undisturbed value close to 0 $m^2 s^{-2}$ to about 0.5 $m^2 s^{-2}$ at all levels. Coincident with the increase in turbulence, the turbulent sensible heat flux toward the surface $\overline{w'T'}$ increased from 0–0.1 to 0.2–0.4 K m s^{-1} (not shown). The cold-air intrusions were intermittent at west upper between 2100 and 0000 MST. During the second half of the night, peak intrusion wind speeds were weaker (typically below 1 m s^{-1}) but still stronger than the undisturbed value of about 0.25 m s^{-1}. The last two events shortly after 0000 MST and shortly before 0300 MST differed from previous ones in that the intrusion wind events occurred with south winds outside the crater rather than southwest winds. This wind direction produced only weak increases in wind speed at west upper. A deep V-shaped

notch formed by the south temperature profile and a less deep notch formed by the west temperature profile (not shown, but similar to Fig. 6b) were consistent with this southerly inflow.

Because the west lower flux tower was embedded within the strong inversion layer that formed on the valley floor, the intrusion penetrated less frequently down to this site. Weak wind speeds and variable directions occurred at this site when the intrusion was not present. The inflow did penetrate to west lower at about 2040 and 2350 MST, as indicated by the peaks in TKE. The intrusions, however, caused only weak increases in wind speeds, to less than 1 m s^{-1}. The intrusions, when they reached west lower, depressed the top of the strong surface-based inversion and increased temperature gradients within the remaining stable layer (Fig. 6a).

4. Conceptual model

From our analyses, we have developed a cold-air intrusion hypothesis that is illustrated in Fig. 9 and is described as follows: At night, a regional-scale drainage
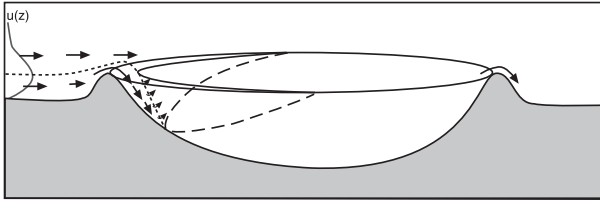
FIG. 9. Illustration of the cold-air intrusion hypothesis. The strongest inflow occurs on the upwind inner sidewall of the crater, with the inflows becoming weaker and penetrating to shallower depths with distance around the crater rim from the upwind direction. The lower limit of the wedge of cold air intruding into the crater across the upwind half of the crater rim is indicated by the heavy dashed line.

flow descends the Colorado Plateau from higher terrain of the Mogollon Rim to the southwest of the crater. The drainage flow splits around the sides of the crater as a cold-air mass builds up on the upwind side of the crater rim (buildup indicated by short-dashed line in Fig. 9). Advection of the cold-air mass up the upwind side of the crater rim causes a shallow layer of cold air to spill over the southwest rim. The coldest air and the largest volume flux come over the rim directly upwind of the crater. The cold air flows down the inner sidewall of the crater as a katabatic current, descending to an altitude corresponding to its temperature deficit and the ambient stability inside the crater. This flow can be considered a katabatic flow coming down a slope but with a continuous source of negatively buoyant air at the top of the slope. The intrusion penetrates deepest into the crater on the upwind inner sidewall, with the penetration depth decreasing to either side of the upwind direction. Detrainment of the cold air into the crater atmosphere from the katabatic flow and its horizontal mixing through the nocturnal inversion destabilizes the crater atmosphere, producing a near-isothermal atmosphere in the upper altitudes of the crater. A weak entrainment of warm air into the intrusion layer from the adjacent crater atmosphere marginally reduces the temperature deficit of the intrusion air. Compensatory rising motions are induced in the crater atmosphere in response to the descent of intrusion air on the upwind inner sidewall. The horizontal mixing processes are not yet fully investigated, but breaking Kelvin–Helmholtz waves at the upper boundary of the katabatic current may play a role, as they do in other gravity currents (Simpson 1997).

Continuous destabilization of the air in the crater is necessary to maintain the near-isothermal temperature structure. The increase of air volume with height in the crater requires more detrainment at the upper altitudes than at the lower altitudes. This is accomplished by the larger volume flux of intrusion air at the upper altitudes of the crater, where the penetration covers a broader swath of the crater periphery. Additionally, the larger temperature deficits occur at the upper altitudes of the crater where the downslope flow of the negatively buoyant air may be enhanced by the steeper sidewall inclination angles. The intruding cold air may produce gravity waves or seiches when it descends far enough down the sidewall to impinge on the top of the intense inversion of about 30–50-m depth on the crater floor. An outflow occurs over the downwind rim in response to the cold-air inflow.

5. Discussion

a. Observations of cold-air intrusions

The identification of the cold-air intrusion phenomenon at Meteor Crater benefited from the extensive network of inexpensive ground-based temperature dataloggers. It would have been difficult to identify the phenomenon solely from the tethered balloon and flux tower data obtained inside the crater. Thus, for future field experiments it is worthwhile to keep in mind the advantages of extensive networks of inexpensive sensors. The rather idealized basin shape of Meteor Crater also assisted in identifying the phenomenon, which might otherwise have been attributed to other processes such as flows coming through major gaps in surrounding topography.

b. Physical processes

The goal of the conceptual model is to explain how cold-air inflow over the rim could destabilize the bulk atmospheric volume inside the crater. This destabilization comes from several competing and interacting processes or mechanisms. First, the destabilization can occur through differential cooling caused by detrainment of cold air from the sidewall. Destabilization would require more cooling per unit width of the basin at the upper altitudes of the crater basin compared to the lower altitudes. Second, rising motions over the center of the crater that compensate for shallow downslope inflow on the sidewall could destabilize the crater atmosphere if the rising motions increased with height. The mathematical basis for this comes from partial differentiation with height of the potential temperature tendency equation for one-dimensional, adiabatic motion,

$$\frac{\partial \gamma}{\partial t} = -\gamma \frac{\partial w}{\partial z} - w \frac{\partial \gamma}{\partial z},$$ (1)

where t is time, z is height, γ is the potential temperature gradient, and w is vertical velocity. The second term on the right-hand side contributes to changes in stability only when the potential temperature gradient varies with height. Third, the inflow brings colder air into the

crater during the course of the night. The decrease of inflow temperature with time, if it were detrained predominantly at the upper elevations, would also act to further destabilize the crater atmosphere. We have developed analytical and numerical models to test the relative importance of these physical processes, including the effects of basin geometry, detrainment, and vertical motion on the temperature structure of the bulk crater atmosphere and its nighttime evolution. A separate paper will be submitted on this topic.

c. Volume flux of the cold-air intrusion

The depth and strength of cold-air inflow over the crater rim have not been measured directly. We can, nonetheless, estimate the inflow volume flux from heat budget considerations by assuming that air flowing over the crater rim will descend into the crater if it is colder than the air already inside the crater. Consider the night of 27 October (Figs. 6d–f). A cold-air inflow that began at 0305 MST changed the stable temperature structure in the crater at that time $[T_1(z)]$ to a near-isothermal structure $[T_2(z)]$ by 0335 MST. The cooling of the crater atmosphere during this short time period is assumed to be driven entirely by the cold-air inflow. A heat budget of the crater atmosphere can then be written as

$$\int_h^H a(z)[T_2(z) - T_1(z)] \, dz = \frac{2}{\pi} \Delta T_{\max} UDL \Delta t, \quad (2)$$

where h is the depth of the shallow inversion on the floor of the crater and H is the height of the crater rim. The left-hand side of the equation is the change in heat content of the crater atmosphere between 0305 and 0335 MST, where $a(z)$ is the horizontal area of the crater, and z is height above the basin floor. The right-hand side gives the cold-air inflow into the crater, where $\Delta T_{\max}$ is the maximum inflow temperature deficit (i.e., the maximum temperature difference between the upwind and downwind rims), $2/\pi$ is a factor that accounts for a cosine-shaped decrease in this maximum temperature difference over the half-circumference of the crater rim [i.e., $\Delta T(x) = \Delta T_{\max} \cos(x\pi/L)$ where x is the distance along an axis perpendicular to the inflow with origin at the crater center], U is the inflow speed, D is the depth of the inflow, L is the crater width, and Δt is the 30-min time difference between 0305 and 0335 MST. This equation can be solved for the inflow volume flux,

$$UD = \frac{\sum_{i=0}^{n} [T_{i+1}(z) - T_i(z)]V(z)}{\frac{2}{\pi} \Delta T_{\max} L \Delta t}, \quad (3)$$

where V is volume. Substituting measured values for the variables in this equation, using $\Delta T_{\max} = 3.9°C$, temperature profiles from the north and south temperature logger lines, and twenty 5-m-deep layers ($n = 19$) results in $UD = 19.7 \text{ m}^2 \text{ s}^{-1}$. This can be met, for example, by an inflow over the crater rim that is 10 m deep, with a mean speed of 2 m s^{-1}.

d. Generality of the cold-air intrusion mechanism

Cold-air intrusions into Meteor Crater are experienced as katabatic flows on the inner sidewalls of the crater. They are different from normal midlatitude katabatic slope flows, which form *in place* on the slope and continue to descend only if continuously cooled by a downward flux of heat to the underlying radiatively cooled surface. In contrast, katabatic flows from the cold-air intrusions are fed by a continuous source of cold air at the *top* of the slope. While these flows may be modified by cooling or heating from the underlying slope, the main driving force for these flows is the continuous cold-air source at the top of the slope.

Cold-air intrusions at Meteor Crater are experienced because of an unusual combination of circumstances. Meteor Crater is located on a regional-scale sloping surface that puts it in the path of a regional-scale downslope cold-air drainage flow. The rim height of the crater is low enough above the adjacent plain that the shallow regional-scale drainage flow can surmount the crater's rim (this would be less likely if the rim were higher). The depth of the crater also allows the katabatic flow to develop on its inner sidewalls. While unusual circumstances allow the cold-air intrusion to be detected at Meteor Crater, these types of flows are likely to be much more widespread. They are difficult to detect in unsaturated flows, but are frequently seen in cloudy or polluted airflows descending through passes or over ridges or other obstacles. They are also detectable as "cold-air avalanches" in complex terrain when cold air builds up on a plateau, mountain top, or basin and is released as a cold-air source at intervals (Kuettner 1949). We must assume that cold-air intrusions are much more common than indicated by cloudy airflows, since clouds are rarely present at the right elevations to visualize these flows. An improved understanding of cold-air intrusions would have important practical implications. Studying their behavior is likely to improve understanding of the transport and dispersion of dense gases in the atmosphere and in other fluid analogs.

6. Summary and conclusions

We present observational evidence that a deep and persistent near-isothermal layer in the upper 75%–80%

of the Meteor Crater atmosphere is produced by turbulence and horizontal mixing associated with a shallow inflow of cold air that comes over the southwest rim of the crater. The inflow is driven by a regional-scale drainage flow that descends the inclined slope from the Mogollon Rim 30 km to the southwest of the crater. The drainage flow develops best on clear nights having weak synoptic-scale influences and piles up cold air on the upwind outer sidewall of the crater while much of the low-level flow is diverted around the crater. A shallow layer of the flow, however, is carried over the crater's southwest rim. The negatively buoyant inflow penetrates into the crater to depths that depend on the temperature deficit of the air coming over the rim, the inflow volume, and the ambient temperature structure inside the crater. The inflows are rarely able to penetrate all the way to the crater floor because of the strong stability in the preexisting, shallow, intense surface-based inversion present in the lower 15%–20% of the crater. A conceptual model of this cold-air inflow, obtained from the analysis of meteorological data collected both inside and outside the crater, is the key contribution of this article. A follow-on paper (Haiden et al. 2010, manuscript submitted to *J. Appl. Meteor. Climatol.*), which starts with this conceptual model and develops an analytical framework to investigate the phenomenon further, especially its effect on ambient atmospheric stability inside the crater and the heat budget of the crater atmosphere, qualitatively confirms the observational findings.

REFERENCES

Baines, P. G., 1999: Downslope flows into a stratified environment—Structure and detrainment. *Mixing and Dispersion in Stably Stratified Flows,* P. A. Davies, Ed., 1–21.

——, 2001: Mixing in flows down gentle slopes into stratified environments. *J. Fluid Mech.,* **443,** 237–270.

——, 2005: Mixing regimes for the flow of dense fluid down slopes into stratified environments. *J. Fluid Mech.,* **538,** 245–267.

Clements, C. B., C. D. Whiteman, and J. D. Horel, 2003: Cold-air-pool structure and evolution in a mountain basin: Peter Sinks, Utah. *J. Appl. Meteor.,* **42,** 752–768.

Kring, D. A., 2007: *Guidebook to the Geology of Barringer Meteorite Crater, Arizona (a.k.a. Meteor Crater)*. LPI Contribution 1355, Lunar and Planetary Institute, 150 pp.

Kuettner, J., 1949: Periodische Luftlawinen (Periodic air avalanches). *Meteor. Rundsch.,* **2,** 183–184.

Savage, L. C., III, S. Zhong, W. Yao, W. J. O. Brown, T. W. Horst, and C. D. Whiteman, 2008: An observational and numerical study of a regional-scale downslope flow in northern Arizona. *J. Geophys. Res.,* **113,** D14114, doi:10.1029/2007JD009623.

Simpson, J. E., 1997: *Gravity Currents in the Environment and the Laboratory*. 2nd ed. Cambridge University Press, 244 pp.

Steinacker, R., and Coauthors, 2007: A sinkhole field experiment in the eastern Alps. *Bull. Amer. Meteor. Soc.,* **88,** 701–716.

Whiteman, C. D., and S. Zhong, 2008: Downslope flows on a low-angle slope and their interactions with valley inversions. Part I: Observations. *J. Appl. Meteor. Climatol.,* **47,** 2023–2038.

——, T. B. McKee, and J. C. Doran, 1996: Boundary layer evolution within a canyonland basin. Part I: Mass, heat, and moisture budgets from observations. *J. Appl. Meteor.,* **35,** 2145–2161.

——, S. Zhong, and X. Bian, 1999: Wintertime boundary-layer structure in the Grand Canyon. *J. Appl. Meteor.,* **38,** 1084–1102.

——, and Coauthors, 2008: METCRAX 2006: Meteorological experiments in Arizona's Meteor Crater. *Bull. Amer. Meteor. Soc.,* **89,** 1665–1680.